

PLASMONIC CHEMISTRY

Quantifying hot carrier and thermal contributions in plasmonic photocatalysis

Linan Zhou¹, Dayne F. Swearer¹, Chao Zhang², Hossein Robatjazi², Hangqi Zhao², Luke Henderson¹, Liangliang Dong¹, Phillip Christopher³, Emily A. Carter⁴, Peter Nordlander^{2,5*}, Naomi J. Halas^{1,2,5*}

Photocatalysis based on optically active, “plasmonic” metal nanoparticles has emerged as a promising approach to facilitate light-driven chemical conversions under far milder conditions than thermal catalysis. However, an understanding of the relation between thermal and electronic excitations has been lacking. We report the substantial light-induced reduction of the thermal activation barrier for ammonia decomposition on a plasmonic photocatalyst. We introduce the concept of a light-dependent activation barrier to account for the effect of light illumination on electronic and thermal excitations in a single unified picture. This framework provides insight into the specific role of hot carriers in plasmon-mediated photochemistry, which is critically important for designing energy-efficient plasmonic photocatalysts.

Numerous recent demonstrations of hot carrier-driven photocatalysis by metal nanoparticles (NPs) that support collective electronic excitations, known as surface plasmons, have greatly stimulated current research activity (1). Hot carriers produced by nonradiative decay of localized surface plasmons can be more energetic than those generated by direct photoexcitation (2). In contrast to semiconductor photocatalysis, a supralinear intensity dependence of photocatalytic reaction rates has been observed in multiple plasmonic photocatalytic reactions, demonstrating higher quantum yields with increasing photon flux (3–5).

In plasmonic photocatalysis, hot carrier-mediated chemical conversion can be synergistic with thermal excitation. For example, for plasmon-mediated O₂ dissociation on Ag cubes, the photocatalytic reaction rate increased exponentially with temperature under constant white-light illumination (5). Recent studies have begun to address the challenge of distinguishing thermal from nonthermal effects (6, 7). The apparent activation barrier for thermal catalysis can be decreased by illumination of a plasmonic photocatalyst (8–10). However, characterization of activation energies under illumination conditions to examine the mechanism of hot carrier-induced activation barrier reduction has been lacking.

We studied the effects of optical illumination on the apparent activation barrier E_a for am-

monia decomposition ($2\text{NH}_3 \rightarrow \text{N}_2 + 3\text{H}_2$) using a plasmonic antenna-reactor (AR) photocatalyst (4). We varied the illumination wavelength λ and intensity I and measured the surface temperature T_s of the photocatalyst pellet with a thermal imaging camera to account for photothermal heating. Our analysis showed that photoinduced reductions of the reaction barrier have an electronic origin. The reaction mechanism of NH₃ decomposition is well studied, with no side reactions (11, 12), and NH₃ is a promising medium for CO₂-free hydrogen storage (13). With conventional thermal catalysis, this application faces substantial challenges because of the high E_a of NH₃ decomposition (1 to 2 eV), which requires high temperatures to achieve a turnover frequency (TOF) of 1 s⁻¹ (one NH₃ molecule per active metal site per second) (14, 15).

Our plasmonic AR photocatalyst was a Cu–Ru surface alloy that consisted of a Cu NP antenna and Ru reactor sites (Cu–Ru–AR) (Fig. 1A), synthesized by coprecipitation (16) with subsequent annealing and reduction in the photoreaction chamber (supplementary materials). The photocatalytic reaction rate on Cu–Ru–AR was ~20 and ~177 times higher, respectively, relative to pure Cu and Ru NPs (Fig. 1B). For illumination at 9.6 W cm⁻², without external heating, the photocatalytic reaction rate of NH₃ decomposition over Cu–Ru–AR was as high as 1200 μmol H₂ g⁻¹ s⁻¹. The reaction rate dropped within the noise of the measurement when the light was turned off. This process was repeated reproducibly multiple (five) times (Fig. 1C). The TOF based on Ru loading was >15 s⁻¹, and the energy efficiency and quantum yield were calculated to be 18 and 33.5%, respectively, under this set of conditions (see supplementary materials for calculation method). The ratio of photocatalytic reaction rates based on the measured amounts of NH₃, N₂, and H₂ were consistent with the stoichiometry of the

reaction, confirming the absence of unintended side reactions.

To differentiate the contributions of plasmon-induced hot electrons and photothermal heating, the steady-state temperature on the photocatalyst surface was measured in situ with a thermal imaging camera (supplementary materials). T_s increased with I and reached 475.4°C at a peak intensity of 9.6 W cm⁻² (fig. S11A). When NH₃ decomposition was performed without illumination, but with external heating temperatures equivalent to those achieved under illumination, the thermocatalytic rates of H₂ production were one to two orders of magnitude below the observed photocatalytic rates (Fig. 1D). Because of limited light penetration into the catalyst pellet (17), the effective amount of catalyst was appreciably smaller for photocatalysis than for thermocatalysis (in the dark). On the basis of this observation, we conclude that plasmon-induced hot carriers are the predominant effect that catalyzes NH₃ decomposition. Although the transient local temperature on the NP surface under illumination can be higher than the static temperature (18), the local temperature was calculated to be less than 0.1 K higher than that of the environment because the energy intensity of each laser pulse was very low (~0.12 μJ cm⁻²) and essentially independent of NP size in this (sub-10-nm-diameter) regime (fig. S12, B to D) (19, 20).

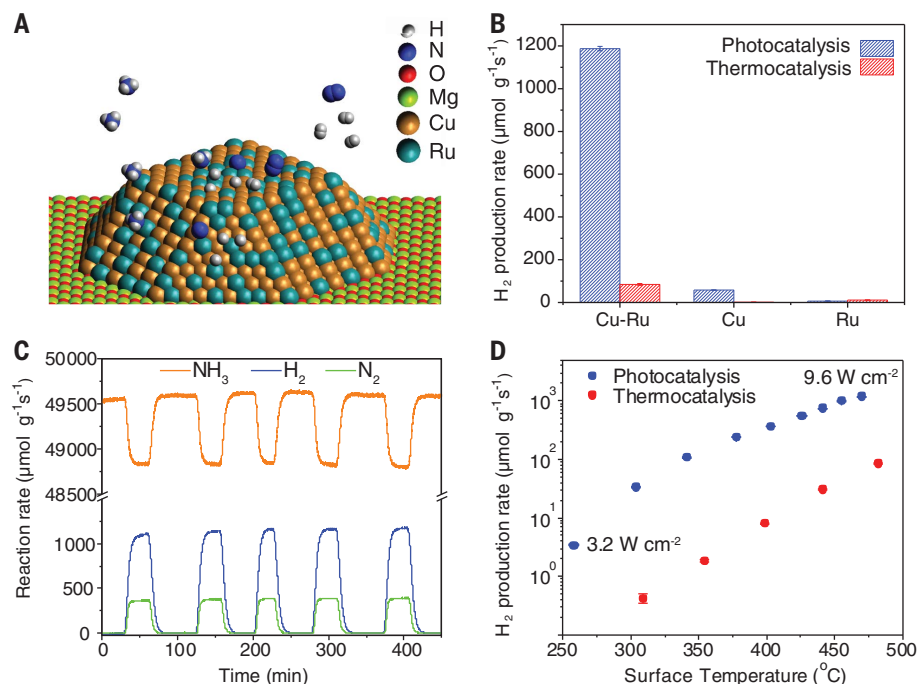
To quantify the effect of illumination on E_a , we measured reaction rates over a range of surface temperatures by varying chamber temperature for each λ and I . We derived $E_a(\lambda, I)$ from the measured reaction rates and T_s values using the Arrhenius equation (table S2). Figure 2, A and B, shows the wavelength dependence of E_a for a fixed I at 3.2 W cm⁻² and the intensity dependence of E_a for a fixed excitation wavelength at 550 nm, corresponding to the localized surface plasmon resonance (LSPR) frequency of the Cu–Ru–AR photocatalyst ($\lambda = 550$ nm, fig. S4). Without light, the E_a was 1.21 eV (black line in Fig. 2A). Illumination on resonance at an intensity of 3.2 W cm⁻² led to the greatest reduction of E_a , from 1.21 to 0.35 eV. For longer λ , the reduction in E_a is less because of reduced optical absorption that decreased hot carrier generation. At shorter λ , the absorption was still high, owing to Cu interband transitions (21), but the reduction in E_a was smaller, because the energetic electrons produced by interband transitions in Cu have substantially lower energies than those produced by plasmon decay (2). This is in contrast to recent observations that more, but less energetic, carriers generated by interband transitions in Au NPs were more efficient than those generated by plasmon resonant excitation in solution phase catalysis (22). In each case, however, the specific energetics of the reaction itself are likely to be very important in ultimately determining photocatalytic efficiencies. For resonant illumination (Fig. 2B), E_a decreased with increasing light intensity. A three-dimensional (3D) contour map of the light-induced E_a (Fig. 2C) shows that the wavelength dependence is similar for all light intensities and that the trend of decreasing E_a with increasing

¹Department of Chemistry, Rice University, Houston, TX 77005, USA. ²Department of Electrical and Computer Engineering, Rice University, Houston, TX 77005, USA. ³Department of Chemical Engineering, University of California, Santa Barbara, Santa Barbara, CA, 93106-5080, USA. ⁴School of Engineering and Applied Science, Princeton University, Princeton, NJ 08544-5263, USA. ⁵Department of Physics and Astronomy, Rice University, Houston, TX 77005, USA.

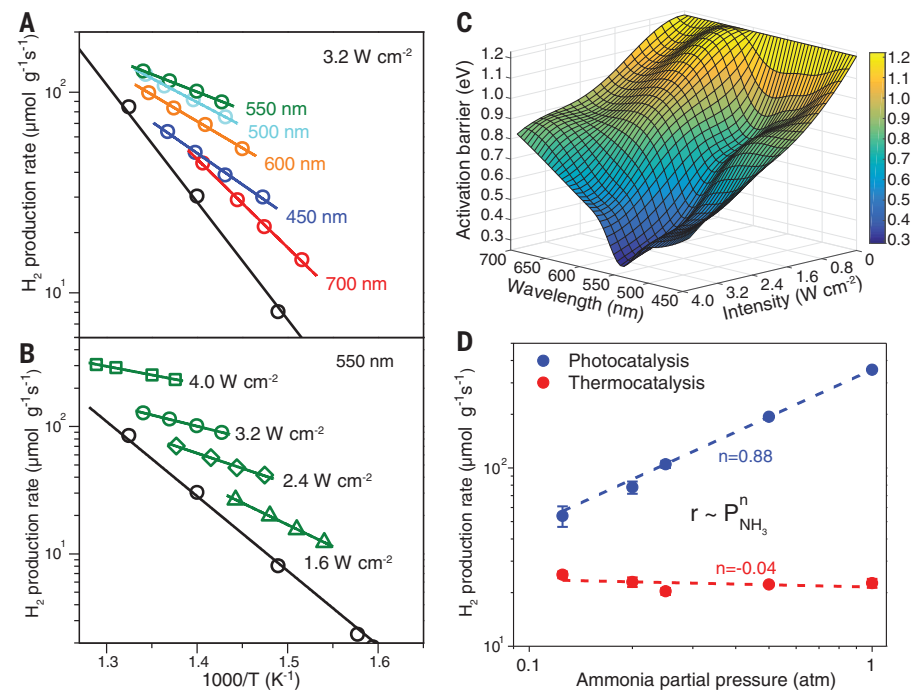
*Corresponding author. Email: nordland@rice.edu (P.N.); halas@rice.edu (N.J.H.)

Fig. 1. Catalytic ammonia decomposition.

(A) Schematic of the structure of Cu-Ru-AR consisting of a Cu NP antenna with a Cu-Ru surface alloy, where the Ru provides the reactor sites. (B) H_2 formation rate of photocatalysis (9.6 W cm^{-2}) and thermocatalysis (482°C) on Cu-Ru-AR, Cu, and Ru NPs. (C) Multiple-hour measurement of photocatalytic rates on Cu-Ru-AR under 9.6 W cm^{-2} white-light illumination without external heating. (D) Comparison of photocatalytic and thermocatalytic rates on Cu-Ru-AR. The horizontal axis corresponds to the surface temperature of the catalyst caused by photothermal heating (photocatalysis) or external heating (thermocatalysis). The light intensity differences between successive data points are 0.8 W cm^{-2} .

**Fig. 2. Light-dependent activation barrier.**

(A and B) Arrhenius plots of apparent activation barriers for (A) different wavelengths under constant intensity of 3.2 W cm^{-2} and (B) various light intensities at 550 nm . The black line represents thermocatalysis in the dark. The surface temperatures of the catalyst were measured with an infrared camera and used for the Arrhenius analysis. (C) A 3D representation of $E_a(\lambda, I)$ for different wavelengths and intensities through interpolation of 46 data points. (D) Reaction order with respect to P_{NH_3} in photocatalysis (6.4 W cm^{-2} white light) and thermocatalysis (427°C). r , H_2 production rate; n , reaction order.



I holds for all λ studied. Under optimal illumination, at the LSPR frequency and an intensity of 4 W cm^{-2} , E_a was reduced to $\sim 0.27 \text{ eV}$.

By mapping E_a as a function of illumination conditions (Fig. 2C), we could predict catalytic performance. For example, according to the Arrhenius curve obtained for 3.2 W cm^{-2} illumination at 550 nm (green line in Fig. 2A), the catalytic reaction rate was calculated to be $22.7 \mu\text{mol H}_2 \text{ g}^{-1} \text{ s}^{-1}$ at 293°C , which is also the T_s for this illumination condition without external heating (fig. S11C). This value was in good agreement with

the measured reaction rate of $19.0 \mu\text{mol H}_2 \text{ g}^{-1} \text{ s}^{-1}$ (fig. S16). Furthermore, because the light-induced heating of nanostructures for arbitrary illumination conditions can be calculated (23, 24), a knowledge of the light-induced $E_a(\lambda, I)$ can provide a direct relation between total energy input and reaction rates. With this insight, it is possible to optimize the efficiency of plasmonic photocatalysis in terms of overall energy efficiency (per mole product divided by per unit energy input).

In the present study, $E_a(\lambda, I)$ was determined by measuring the T_s of the catalyst during the

reaction, making it possible to clearly distinguish the hot carrier contributions from photothermal heating. In situations where the temperature change of the catalyst cannot be determined independently or through calculations, the measured light dependence of the activation barrier will also include contributions from photothermal heating. In the supplementary materials, we discuss how the intrinsic light-dependent barrier can be determined from the measured barrier in that case.

The E_a of a reaction is defined as the sum of the activation barriers for the rate-determining

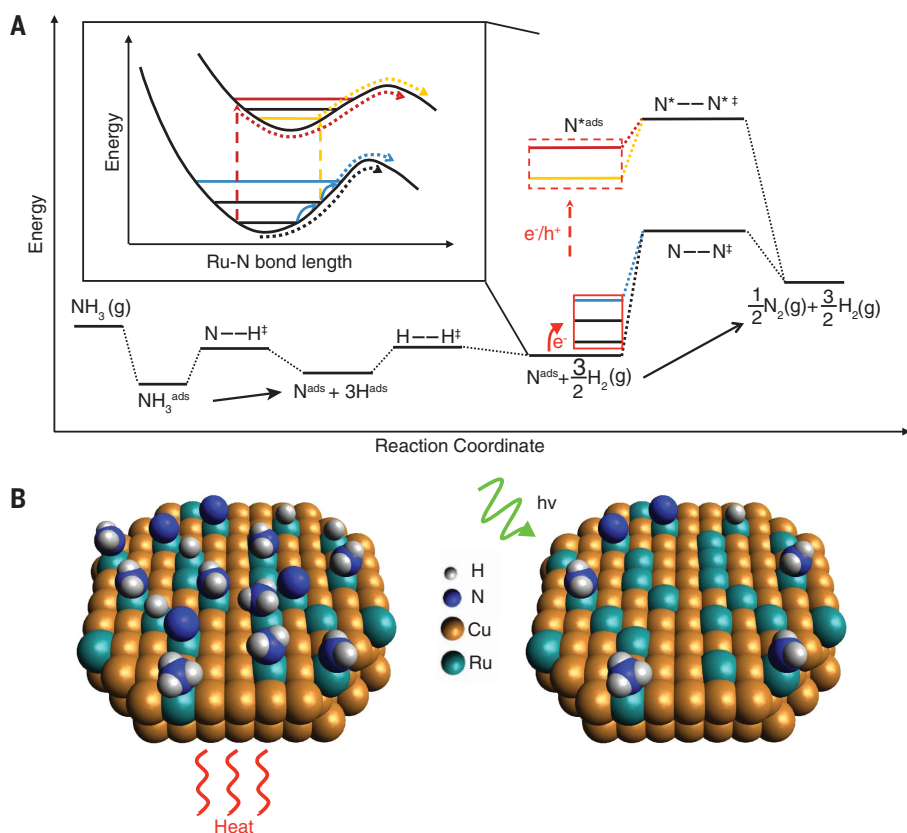


Fig. 3. Mechanisms for hot carrier-mediated reduction of activation barrier. (A) Schematic energetics of elementary reaction steps for NH_3 decomposition. The \ddagger denotes transition state, and the two relevant RDSs, N-H bond scission and associative desorption of N_2 , are labeled. N^* refers to excited Ru-N surface species: either vibronic levels in an excited electronic state (red dashed arrow and box) or vibrational excitations in the electronic ground state (red solid arrow and box). The activation barriers after excitation (red, yellow, and blue dotted lines) are all lower than that of the ground state (black dotted line). The Franck-Condon diagram inset illustrates the mechanisms in more detail. Dark red and yellow dashed arrows denote possible hot carrier transfer into or electronic excitation of the Ru-N surface species. Blue solid arrows denote multiple vibrational excitations of the electronic ground state. e^- , electron; h^+ , hole. (B) Schematics of surface coverage under heating versus light-illumination conditions. In contrast to thermocatalysis (left), photocatalysis and hot carrier generation (right) can promote desorption of “poisoning” adsorbed intermediates. $h\nu$, light.

step (RDS) ($E_{a\text{-RDS}}$), the enthalpy of the steps that produce species involved in the RDS, and a coverage-dependent term related to the enthalpy required to clean active sites occupied by reaction intermediates (25). For NH_3 decomposition on a Ru surface, there are two reported RDSs: (i) N-H bond scission (one of the three N-H breaking steps) and (ii) associative desorption of N_2 (26, 27). Measurements of the reaction rate dependence on NH_3 partial pressure (P_{NH_3}) show a zeroth order dependence for the thermocatalytic reaction and a first-order dependence for the photocatalytic reaction (Fig. 2D). In the thermocatalytic experiments, the RDS is the associative desorption of N_2 , with the reaction intermediates, mostly N, adsorbed on the surface, blocking reaction sites (28, 29). This model was confirmed by the large measured E_a (1.21 eV), which stems from the sum of $E_{a\text{-RDS}}$ and the energy penalty associated with cleaning active sites occupied by adsorbed intermediates. For photocatalysis with 6.4 W cm^{-2} white-light illumination (T_s of 403°C , fig. S11B), the reaction order with respect to P_{NH_3} increased substantially, to 0.88. This increase in reaction order, along with a reduction in E_a upon illumination, suggests that hot carriers induced by resonant illumination modify the reaction kinetics by reducing the activation barrier for associative desorption of N_2 ($E_{a\text{-RDS}}$), while simultaneously decreasing the surface coverage of adsorbed intermediates. It is plausible that higher-intensity illumination shifted the RDS from associative desorption of N_2 to N-H bond scission. Both processes decrease E_a , syn-

ergistically promoting efficient plasmon-mediated NH_3 decomposition.

Hot carriers can influence the energetics of adsorbed N (N^{ads}) and enhance the net reaction rate, as verified by an analysis of the microkinetics for this reaction (30) discussed in the supplementary materials. More importantly, the $E_{a\text{-RDS}}$, and thus the E_a , can be reduced by activating the N^{ads} through hot carriers, in many ways, along the reaction pathway (Fig. 3A). Hot electrons and holes can transfer into N^{ads} and electronically excite the Ru-N surface species, thus facilitating the N_2 desorption process (red dashed arrow in Fig. 3A). The Ru-N bond activation then occurs through an excited state with a lower activation barrier (dark red and yellow dotted lines in Fig. 3A). This process requires resonant conditions between the hot carriers and the acceptor levels of the Ru-N surface species (dark red and yellow dashed arrows in the inset). Once created by plasmon decay, hot carriers rapidly relax toward the Fermi level through a carrier multiplication process induced by electron-electron scattering (31). Electron-phonon scattering on a monometallic particle plays a relatively minor role, because such phonons involve atoms of the same charges and do not possess electrical multipolar moments. However, the interaction can be strong for localized vibrational modes involving atoms of different charges, such as the Ru-N surface species.

Thus, another possibility for activation of the Ru-N bond is inelastic electron-vibrational dipole scattering (red solid arrow in Fig. 3A). This pro-

cess does not require resonant conditions and can occur as long as the hot carriers have energies greater than the vibrational quantum. The excited electrons can induce multiple vibrational transitions of the Ru-N bond (blue solid arrows in the Franck-Condon diagram inset in Fig. 3A), and as the vibrational energy stored in the bond increases, the activation energy is reduced. In particular, a recent report showed that the excited vibrational state of surface species could exhibit 100-ps-long lifetimes and thus assist the barrier-crossing process (32). Overall, both excitations (hot carrier, energy transfer, and electron-vibrational scattering) could contribute to accelerating the associative desorption of N_2 , which has been described previously as desorption induced by electronic transitions (DIET) on metal substrates under light excitation (33–36). With more molecules excited to higher vibronic states by higher light intensities, closer-to-resonant photoexcitation, or both processes, the $E_{a\text{-RDS}}$ decreases, as does the E_a of the entire reaction. Although the DIET mechanism would also apply to other species such as H_2 , desorption of these species is not the RDS here and would have little effect on the E_a . Hot carrier-induced desorption of intermediates (Fig. 3B) also contributes to the decrease of E_a by decreasing the coverage of intermediates and releasing the active sites, as discussed in the supplementary materials.

REFERENCES AND NOTES

1. Y. Zhang et al., *Chem. Rev.* **118**, 2927–2954 (2017).
2. B. Y. Zheng et al., *Nat. Commun.* **6**, 7797 (2015).

3. C. Zhang *et al.*, *Nano Lett.* **16**, 6677–6682 (2016).
4. D. F. Swearer *et al.*, *Proc. Natl. Acad. Sci. U.S.A.* **113**, 8916–8920 (2016).
5. P. Christopher, H. Xin, A. Marimuthu, S. Linic, *Nat. Mater.* **11**, 1044–1050 (2012).
6. X. Zhang *et al.*, *Nano Lett.* **18**, 1714–1723 (2018).
7. Y. Yu, V. Sundaresan, K. A. Willets, *J. Phys. Chem. C* **122**, 5040–5048 (2018).
8. X. Zhang *et al.*, *Nat. Commun.* **8**, 14542 (2017).
9. H. Song *et al.*, *ACS Appl. Mater. Interfaces* **10**, 408–416 (2018).
10. Y. Kim, D. Dumett Torres, P. K. Jain, *Nano Lett.* **16**, 3399–3407 (2016).
11. G. Ertl, M. Huber, *J. Catal.* **61**, 537–539 (1980).
12. M. C. J. Bradford, P. E. Fanning, M. A. Vannice, *J. Catal.* **172**, 479–484 (1997).
13. T. E. Bell, L. Torrente-Murciano, *Top. Catal.* **59**, 1438–1457 (2016).
14. F. Schüth, R. Palkovits, R. Schlögl, D. S. Su, *Energy Environ. Sci.* **5**, 6278–6289 (2012).
15. A. Amano, H. Taylor, *J. Am. Chem. Soc.* **76**, 4201–4204 (1954).
16. M. Behrens, *Catal. Today* **246**, 46–54 (2015).
17. H. Robatjazi *et al.*, *Nat. Commun.* **8**, 27 (2017).
18. V. K. Pustovalov, *Chem. Phys.* **308**, 103–108 (2005).
19. A. M. Goodman *et al.*, *ACS Nano* **11**, 171–179 (2017).
20. S. C. Nguyen *et al.*, *ACS Nano* **10**, 2144–2151 (2016).
21. G. H. Chan, J. Zhao, E. M. Hicks, G. C. Schatz, R. P. Van Duyne, *Nano Lett.* **7**, 1947–1952 (2007).
22. J. Zhao *et al.*, *ACS Cent. Sci.* **3**, 482–488 (2017).
23. H. I. Villafán-Vidales, S. Abanades, C. Caliot, H. Romero-Paredes, *Appl. Therm. Eng.* **31**, 3377–3386 (2011).
24. F. J. Valdés-Parada, H. Romero-Paredes, G. Espinosa-Paredes, *Int. J. Hydrogen Energy* **36**, 3354–3363 (2011).
25. H. Lynggaard, A. Andreasen, C. Stegelmann, P. Stoltze, *Prog. Surf. Sci.* **77**, 71–137 (2004).
26. W. Tsai, W. H. Weinberg, *J. Phys. Chem.* **91**, 5302–5307 (1987).
27. C. Egawa, T. Nishida, S. Naito, K. Tamaru, *J. Chem. Soc., Faraday Trans. I* **80**, 1595–1604 (1984).
28. A. Hellman *et al.*, *Surf. Sci.* **603**, 1731–1739 (2009).
29. V. Prasad, A. M. Karim, A. Arya, D. G. Vlachos, *Ind. Eng. Chem. Res.* **48**, 5255–5265 (2009).
30. C. T. Campbell, *ACS Catal.* **7**, 2770–2779 (2017).
31. J. G. Liu, H. Zhang, S. Link, P. Nordlander, *ACS Photonics* **5**, 2584–2595 (2017).
32. P. R. Shirhatti *et al.*, *Nat. Chem.* **10**, 592–598 (2018).
33. H. L. Dai, W. Ho, *Laser Spectroscopy and Photochemistry on Metal Surfaces* (World Scientific, 1995).
34. C. Frischkorn, M. Wolf, *Chem. Rev.* **106**, 4207–4233 (2006).
35. S. A. Buntin, L. J. Richter, R. R. Cavanagh, D. S. King, *Phys. Rev. Lett.* **61**, 1321–1324 (1988).
36. V. A. Spata, E. A. Carter, *ACS Nano* **12**, 3512–3522 (2018).

ACKNOWLEDGMENTS

Funding: This research was financially supported by the Air Force Office of Scientific Research Multidisciplinary Research Program

of the University Research Initiative (MURI FA9550-15-1-0022) (P.C., E.A.C., P.N., and N.J.H.) and the Welch Foundation under grants C-1220 (N.J.H.) and C-1222 (P.N.). D.F.S. acknowledges the National Science Foundation for a Graduate Research Fellowship under grant no. 1450681. **Author contributions:** L.Z. developed the nanoparticle synthesis; L.Z., D.F.S., C.Z., H.R., L.H., and L.D. performed the physical characterization of the nanoparticles and the photocatalysis studies; H.Z. performed the theoretical simulations. All authors analyzed and interpreted the results and contributed to the preparation of the manuscript. P.N. and N.J.H. supervised the research. **Competing interests:** N.J.H., P.N., D.F.S., H.Z., H.R., C.Z., and L.Z. are coinventors on the provisional patent application relating to the research presented in this paper. **Data and materials availability:** All data needed to evaluate the conclusions in the paper are available in the manuscript or the supplementary materials.

SUPPLEMENTARY MATERIALS

www.sciencemag.org/content/362/6410/69/suppl/DC1
Materials and Methods
Supplementary Text
Figs. S1 to S17
Tables S1 and S2
References (37–44)

26 March 2018; accepted 15 August 2018
10.1126/science.aat6967